Motion gradients for epipolar consistency

Alexander Preuhs[a*], **Michael Manhart**[b], **Elisabeth Hoppe**[a], **Markus Kowarschik**[b], **Andreas Maier**[a]
[a]Pattern Recognition Lab, Friedrich-Alexander-Universität Erlangen-Nürnberg, Germany
[b]Siemens Healthcare GmbH, Forchheim, Germany

Abstract. Enforcing geometric consistency of an acquired cone-beam computed tomography scan has been shown to be a promising approach for online geometry calibration and the compensation of rigid patient motion. The approach estimates the motion parameters by solving an optimization problem, where the cost function is the accumulated consistency based on Grangeat's theorem. In all previous work, this is performed with zero-order optimization methods like the Nelder-Mead algorithm or grid search. We present a derivation of motion gradients enabling the usage of more efficient first-order optimization algorithms for the estimation of rigid patient motion or geometry misalignment. We first present a general formulation of the gradients, and explicitly compute the gradient for the longitudinal patient axis. To verify our results, we compare the presented analytic gradient with a finite difference. In a second experiment we compare the computational demand of the presented gradient with the finite differences. The analytic gradient clearly outperforms the finite differences with a speed up of ~ 35 %.

1 Introduction

In neuroradiology, 3-D imaging with an interventional C-arm cone-beam computed tomography (CBCT) system can enable a reduced time-to-therapy.[1] By replacing the conventional CT scan, diagnosis and treatment for stroke therapy can be performed on the same system. A drawback is the prolonged acquisition time and inherently resulting amplified patient motion.

Grangeat's theorem[2] can be used to compare redundant areas in the acquired projections. Rigid motion defects the redundancy measure and the projections reveal inconsistency. Thus, Grangeat's theorem can be used for restoring consistency by estimating motion parameters using the raw projection data only. The consistency measure was applied for the compensation of geometric jitter.[3,4] Frysch et al. proposed an optimization scheme utilizing Grangeat's theorem for head motion compensation based on the Nelder-Mead method[5] and Preuhs et al. introduced symmetry priors for the estimation of head motion with Grangeat's consistency.[6]

All methods utilize zero-order optimization, by successively evaluating the consistency with different motion configurations. In this work, we derive motion gradients for the estimation of motion parameters with Grangeat's theorem, enabling first-order optimization algorithms. We derive a general formulation based on epipolar consistency (EC) and explicitly compute the gradient for the longitudinal patient direction.

2 Methods

The comparison of redundant data based on Grangeat's theorem is performed by finding pairs of epipolar lines in two projections defined by their projection matrix P_a, P_b and the measured raw data. A transformation of these two lines must be equal according to Grangeat's theorem. We denote the transformed value Consistency Intermediate Value (CIV) which can be precomputed as a look-up-table (LUT) for each projection[7,8] from the measured raw data. The LUT is a (filtered) transformation of the projection domain to the sinogram domain. The sinogram domain is parameterized by a u-direction, which describes the offset of a line, and a v-direction, describing the orientation of a line. Thus, the CIV corresponding to an epipolar line — defined by angle

and offset — is found at the respective u and v coordinate on the LUT. Aichert et al. presented an efficient algorithm[8] to evaluate the consistency by comparing CIV pairs. It is based on a plane rotating around the line connecting two source positions $\vec{s}_\diamond$ with $\diamond \in a, b$. The epipolar lines are found by intersecting the planes with the detectors. With the line parameters $\kappa_1^\diamond$,$\kappa_2^\diamond$ and $\kappa_3^\diamond$, the CIV value of both lines can be looked up by computing the u and v values from the line using the mapping functions $\phi_u^\diamond$ and $\phi_v^\diamond$. The distance between the two CIV values determines the epipolar consistency. We use the robust Geman-McClure norm as distance measure. Therefore, we define the consistency as $\mathrm{ECC}(\vec{x}) = \frac{\mathrm{d}(\vec{x})^2}{1+\sigma\,\mathrm{d}(\vec{x})^2}$ where $\mathrm{d}(\vec{x})$ is the difference of the respective CIV values $\mathrm{d}(\vec{x}) = F_a(u_a(\vec{x}), v_a(\vec{x})) - F_b(u_a(\vec{x}), v_b(\vec{x}))$ and $\vec{x}$ defines the motion parameters. The partial derivatives of the consistency measure are defined by

$$\frac{\partial\,\mathrm{ECC}(\vec{x})}{\partial x_i} = \frac{2\,\mathrm{d}(\vec{x})}{(\sigma \mathrm{d}(\vec{x})^2+1)^2}\left(\frac{\partial F_a(u_a(\vec{x}), v_a(\vec{x}))}{\partial x_i} - \frac{\partial F_b(u_b(\vec{x}), v_b(\vec{x}))}{\partial x_i}\right) \quad . \tag{1}$$

The right part of Eq. (1) is computed as $\frac{\partial F_\diamond(u_\diamond(\vec{x}),v_\diamond(\vec{x}))}{\partial x_i} = \frac{\partial F(\vec{\phi}^\diamond(\vec{x}))}{\partial \phi_u^\diamond(\vec{x})}\frac{\partial \phi_u^\diamond(\vec{x})}{\partial x_i} + \frac{\partial F(\vec{\phi}^\diamond(\vec{x}))}{\partial \phi_v^\diamond(\vec{x})}\frac{\partial \phi_v^\diamond(\vec{x})}{\partial x_i}$. This describes the partial derivatives of the LUT containing the CIVs, and the partial derivatives of the mapping function w.r.t. u and v, respectively. The partial derivatives of the CIVs is obtained as central differences of the LUT. With the mapping functions being defined by $\phi_u^\diamond(\vec{x}) = \frac{\kappa_3^\diamond(\vec{x})}{\sqrt{\kappa_1^\diamond(\vec{x})^2+\kappa_2^\diamond(\vec{x})^2}}$ and $\phi_v^\diamond(\vec{x}) = \mathrm{atan2}(\kappa_1^\diamond(\vec{x}), \kappa_2^\diamond(\vec{x}))$, the partial derivatives are defined as

$$\frac{\partial \phi_u^\diamond(\vec{x})}{\partial x_i} = \frac{\frac{\partial \kappa_3^\diamond(\vec{x})}{\partial x_i}}{\sqrt{\kappa_1^\diamond(\vec{x})^2+\kappa_2^\diamond(\vec{x})^2}} - \frac{\kappa_3^\diamond(\vec{x})\left(\kappa_1^\diamond(\vec{x})\frac{\partial \kappa_1^\diamond(\vec{x})}{\partial x_i} + \kappa_2^\diamond(\vec{x})\frac{\partial \kappa_2^\diamond(\vec{x})}{\partial x_i}\right)}{(\kappa_1^\diamond(\vec{x})^2+\kappa_2^\diamond(\vec{x})^2)^{\frac{3}{2}}} \tag{2}$$

$$\frac{\partial \phi_v^\diamond(\vec{x})}{\partial x_i} = \frac{\kappa_1^\diamond(\vec{x})\frac{\partial \kappa_2^\diamond(\vec{x})}{\partial x_i} - \frac{\partial \kappa_1^\diamond(\vec{x})}{\partial x_i}\kappa_2^\diamond(\vec{x})}{\kappa_1^\diamond(\vec{x})^2+\kappa_2^\diamond(\vec{x})^2} \quad . \tag{3}$$

In the following we restrict our derivation to the gradient in t_z direction and w.l.o.g. assume that projection a is moving, while projection b remains static. Preuhs et al. proposed to replace the projection of a plane with the projection of a line at infinity.[9] This is constructed as the incident of the plane with the plane at infinity, which allows to define new projection matrices $\tilde{P}^\diamond$ defined as

$$\tilde{P}^\diamond = \begin{pmatrix} \tilde{p}_{11}^\diamond & \tilde{p}_{1,2}^\diamond & \tilde{p}_{1,3}^\diamond \\ \tilde{p}_{21}^\diamond & \tilde{p}_{2,2}^\diamond & \tilde{p}_{2,3}^\diamond \\ \tilde{p}_{31}^\diamond & \tilde{p}_{3,2}^\diamond & \tilde{p}_{3,3}^\diamond \end{pmatrix} = \begin{pmatrix} p_{22}^\diamond p_{33}^\diamond - p_{23}^\diamond p_{32}^\diamond & p_{23}^\diamond p_{31}^\diamond - p_{21}^\diamond p_{33}^\diamond & p_{21}^\diamond p_{32}^\diamond - p_{22}^\diamond p_{31}^\diamond \\ p_{12}^\diamond p_{33}^\diamond - p_{13}^\diamond p_{32}^\diamond & p_{13}^\diamond p_{31}^\diamond - p_{11}^\diamond p_{33}^\diamond & p_{11}^\diamond p_{32}^\diamond - p_{12}^\diamond p_{31}^\diamond \\ p_{12}^\diamond p_{23}^\diamond - p_{13}^\diamond p_{22}^\diamond & p_{13}^\diamond p_{21}^\diamond - p_{11}^\diamond p_{23}^\diamond & p_{11}^\diamond p_{22}^\diamond - p_{12}^\diamond p_{21}^\diamond \end{pmatrix} \quad . \tag{4}$$

Exploiting Eq. (4) the line parameters for the mapping functions (cf. Eq. (2),(3)) are derived as

$$\kappa_1^\diamond(t_z) = a(t_z)\tilde{p}_{11}^\diamond + b(t_z)\,\tilde{p}_{12}^\diamond + c(t_z)\,\tilde{p}_{13}^\diamond \tag{5}$$

$$\kappa_2^\diamond(t_z) = a(t_z)\tilde{p}_{21}^\diamond + b(t_z)\,\tilde{p}_{22}^\diamond + c(t_z)\,\tilde{p}_{23}^\diamond \tag{6}$$

$$\kappa_3^\diamond(t_z) = a(t_z)\tilde{p}_{31}^\diamond + b(t_z)\,\tilde{p}_{32}^\diamond + c(t_z)\,\tilde{p}_{33}^\diamond \quad , \tag{7}$$

where the parameters $a(t_z), b(t_z)$ and $c(t_z)$ describe the normal of the epipolar plane w.r.t. a t_z translation of projection a. With $s_{a,i}$ being the components of the source position $\vec{s}_a$, the plane normals are computed as

$$a(t_z) = (q\,s_{a,3} - p s_{a,2} - q t_z + r) \tag{8}$$

$$b(t_z) = (p\,s_{a,1} - s\,s_{a,3} + s\,t_z + t) \tag{9}$$

$$c(t_z) = (s\,s_{a,2} - q\,s_{a,1} - u) \quad , \tag{10}$$

where p, q, r, s, t, u are the Plücker[8,9] coordinates of a line incident to the epipolar plane independent of t_z — typically incident to $\vec{s}_b$. To evaluate Eq. (2) and (3) we further need the partial derivatives of Eq. (8)-(10) w.r.t. t_z defined by

$$\frac{\partial \kappa_1^\diamond(t_z)}{\partial t_z} = \frac{\partial a(t_z)}{\partial t_z}\tilde{p}_{11}^\diamond + \frac{\partial b(t_z)}{\partial t_z}\tilde{p}_{12}^\diamond + \frac{\partial c(t_z)}{\partial t_z}\tilde{p}_{13}^\diamond \tag{11}$$

$$\frac{\partial \kappa_2^\diamond(t_z)}{\partial t_z} = \frac{\partial a(t_z)}{\partial t_z}\tilde{p}_{21}^\diamond + \frac{\partial b(t_z)}{\partial t_z}\tilde{p}_{22}^\diamond + \frac{\partial c(t_z)}{\partial t_z}\tilde{p}_{23}^\diamond \tag{12}$$

$$\frac{\partial \kappa_3^\diamond(t_z)}{\partial t_z} = \frac{\partial a(t_z)}{\partial t_z}\tilde{p}_{31}^\diamond + \frac{\partial b(t_z)}{\partial t_z}\tilde{p}_{32}^\diamond + \frac{\partial c(t_z)}{\partial t_z}\tilde{p}_{33}^\diamond \ , \tag{13}$$

where the derivatives of the plane normal are defined by

$$\frac{\partial a(t_z)}{\partial t_z} = -q \qquad \frac{\partial b(t_z)}{\partial t_z} = s \qquad \frac{\partial c(t_z)}{\partial t_z} = 0 \ . \tag{14}$$

This defines all components need to compute the motion gradient in t_z direction defined by Eq. (1).

3 Evaluation and results

Numeric proof of gradient. To verify our results we implemented the t_z gradient for EC in OpenCL using the software framework CONRAD.[10] The gradient is evaluated at different t_z translations simulating patient head motion. Therefore, we have acquired a short scan of a head phantom with a robotic C-arm system (Artis zeego, Siemens Healthcare GmbH, Germany) and manipulated the projection matrices. The simulated motion ranges from -0.5 mm to 0.5 mm. To verify the results, the finite differences based on the conventional EC[8] are computed using central differences. Both curves are depicted in Fig. 1. It can be observed, that the analytic gradient is slightly closer to zero at the motion free — ground truth — position ($t_z = 0$).

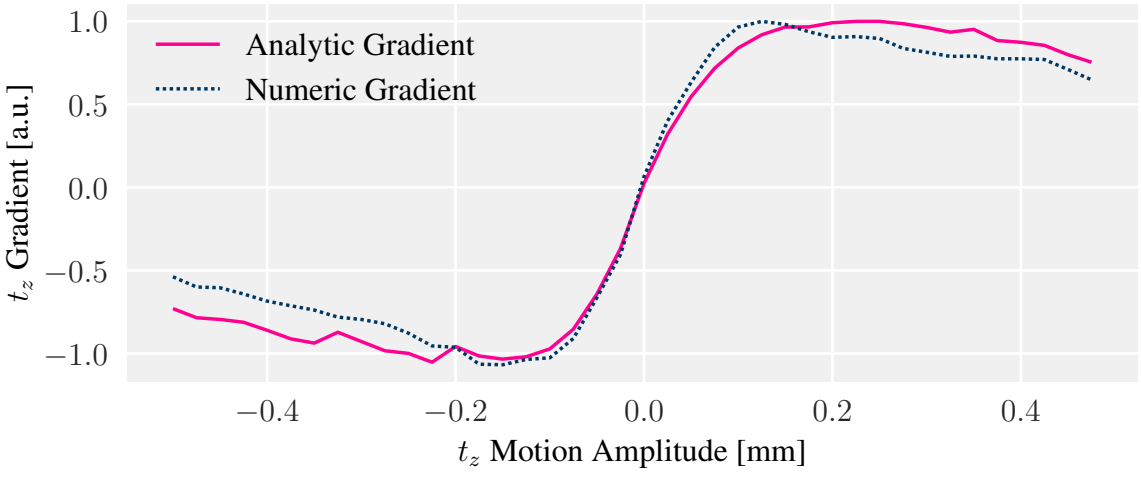

Fig 1 Numeric proof of derived t_z gradient.

Runtime comparison. In a second experiment we compared the runtime of the analytic with the numeric gradient. Both gradients are implemented on the GPU. We have measured the duration of 100 function calls, on a dataset consisting of 248 projections. On average, a single function call of the numeric gradient has a runtime of 120 ± 1 ms, and the analytic gradient of 85 ± 1 ms.

4 Discussion

We have proposed a general formulation of motion gradients for EC and explicitly derived the t_z motion gradient. The profile of the analytic and numeric gradient is as expected very similar, but the numeric gradient is a bit smoother. Other imaging artifacts as scatter or beam hardening degrade the EC and appear as noise in the gradient.[7] This is observable in the analytic gradient, whereas the approximation characteristics of the finite differences reveal a smoothed curve.

While current literature utilizes zero-order optimization only, the proposed motion gradients enable first-order optimization strategies. Motion estimation using EC is challenging due to its inherent sensitivity depending on the motion direction. Therefore, specialized optimization strategies must be applied.[5] The provided gradients of this work have the potential to further improve the optimization schemes to provide high image quality also in the presence of rigid patient motion.
Disclaimer: The concepts and information presented in this paper are based on research and are not commercially available.

Keywords: Grangeat, epipolar consisntecy, interventional imaging, motion.

***Corresponding author, alexander.preuhs@fau.de

References

1 M. Psychogios, D. Behme, K. Schregel, *et al.*, "One-stop management of acute stroke patients: Minimizing door-to-reperfusion times," *Stroke* (2017).
2 M. Defrise and R. Clack, "A Cone-Beam Reconstruction Algorithm Using Shift-Variant Filtering and Cone-Beam Backprojection," *TMI* **13**(1) (1994).
3 C. Debbeler, N. , M. Elter, *et al.*, "A New CT Rawdata Redundancy Measure applied to Automated Misalignment Correction," *Fully 3D* (2013).
4 N. Maass, F. Dennerlein, A. Aichert, *et al.*, "Geometrical Jitter Correction in CT," *CT-Meeting* (2014).
5 R. Frysch and G. Rose, "Rigid motion compensation in C-arm CT using consistency measure on projection data," *MICCAI* (2015).
6 A. Preuhs, A. Maier, M. Manhart, *et al.*, "Double your views – exploiting symmetry in transmission imaging," *MICCAI* (2018).
7 A. Preuhs, R. Nishant, M. Manhart, *et al.*, "Maximum likelihood estimation of head motion using epipolar consistency," *CT-Meeting* (2018).
8 A. Aichert, M. Berger, J. Wang, *et al.*, "Epipolar Consistency in Transmission Imaging," *TMI* **34**(11) (2015).
9 A. Preuhs, M. Manhart, and A. Maier, "Fast Epipolar Consistency without the Need for Pseudo Matrix Inverses," *CT-Meeting* (2018).
10 A. Maier, H. Hofmann, M. Berger, *et al.*, "CONRAD - A software framework for cone-beam imaging in radiology," *Medical Physics* **40**(11) (2013).